The Company of **Biologists**

RESEARCH ARTICLE

Latching of the click beetle (Coleoptera: Elateridae) thoracic hinge enabled by the morphology and mechanics of conformal structures

Ophelia Bolmin[1], Lihua Wei[1], Alexander M. Hazel[2], Alison C. Dunn[1], Aimy Wissa[1,*] and Marianne Alleyne[3]

ABSTRACT

Elaterid beetles have evolved to 'click' their bodies in a unique maneuver. When this maneuver is initiated from a stationary position on a solid substrate, it results in a jump not carried out by the traditional means of jointed appendages (i.e. legs). Elaterid beetles belong to a group of organisms that amplify muscle power through morphology to produce extremely fast movements. Elaterids achieve power amplifications through a hinge situated in the thoracic region. The actuating components of the hinge are a peg and mesosternal lip, two conformal parts that latch to keep the body in a brace position until their release, the 'click', that is the fast launch maneuver. Although prior studies have identified this mechanism, they were focused on the ballistics of the launched body or limited to a single species. In this work, we identify specific morphological details of the hinges of four click beetle species – *Alaus oculatus*, *Parallelostethus attenuatus*, *Lacon discoideus* and *Melanotus* spp. – which vary in overall length from 11.3 to 38.8 mm. Measurements from environmental scanning electron microscopy (ESEM) and computerized tomography (CT) were combined to provide comparative structural information on both exterior and interior features of the peg and mesosternal lip. Specifically, ESEM and CT reveal the morphology of the peg, which is modeled as an Euler–Bernoulli beam. In the model, the externally applied force is estimated using a micromechanical experiment. The equivalent stiffness, defined as the ratio between the applied force and the peg tip deflection, is estimated for all four species. The estimated peg tip deformation indicates that, under the applied forces, the peg is able to maintain the braced position of the hinge. This work comprehensively describes the critical function of the hinge anatomy through an integration of specific anatomical architecture and engineering mechanics for the first time.

KEY WORDS: Click beetles, Hinge mechanics, Hinge morphology, Power amplification

INTRODUCTION

The maneuverability of insects is enabled, in part, by sophisticated energy storage and release processes involving composite materials and architectures (Gronenberg, 1996). These energy storage and release processes allow for extremely fast movements for hunting, escape or other behaviors, as is the case for trap-jaw ants (Hymenoptera: Formicidae), springtails (Collembola) (Larabee

[1]Department of Mechanical Science and Engineering, University of Illinois at Urbana-Champaign, Urbana, IL 61801, USA. [2]Orpheum Children's Science Museum, Champaign, IL 61820, USA. [3]Department of Entomology, School of Integrative Biology, University of Illinois at Urbana-Champaign, Urbana, IL 61801, USA.

*Author for correspondence (awissa@illinois.edu)

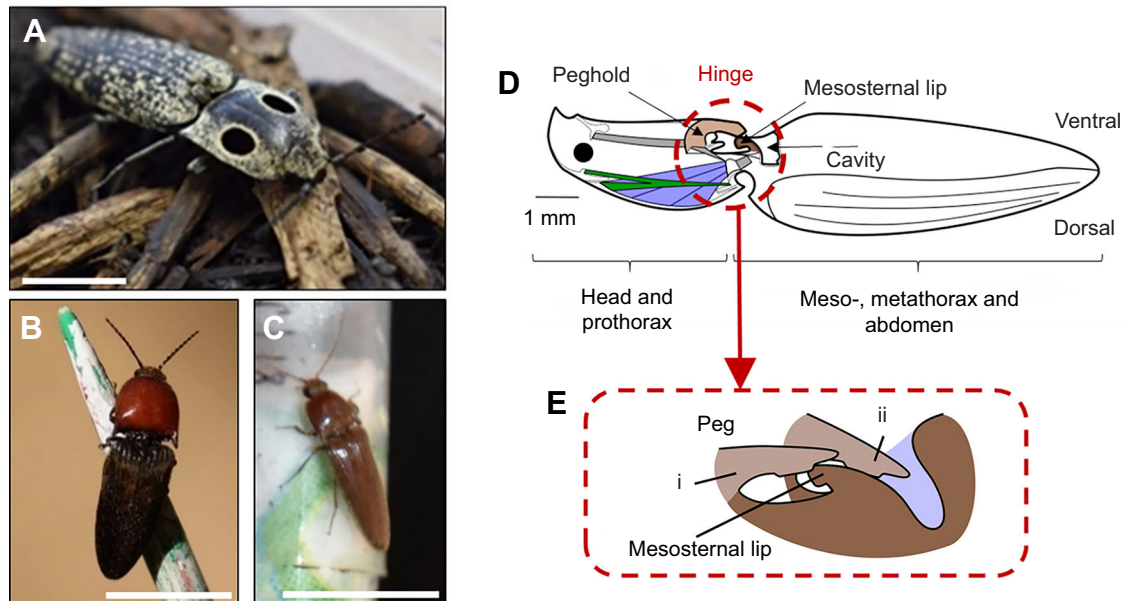A.M.H., 0000-0001-5430-565X; A.W., 0000-0002-8468-511X

et al., 2017) and mantis shrimps (Patek et al., 2007). Click beetles (Coleoptera: Elateridae) (Fig. 1A–C) use a hinge mechanism in the thoracic region to snap their bodies, which, when unconfined, manifests as a jump (Evans, 1972; Ribak et al., 2013). All these organisms use power amplification mechanisms to achieve extremely high accelerations. Common power amplification mechanisms include a latch to allow for elastic energy storage over an extended period and a quick snap/release to expend the stored energy over a much shorter time. This variation in time between the energy storage and release allows for the amplification of power output. Understanding how a body, such as that of a click beetle, can accelerate from a stationary position without using legs requires an integrated description of the morphology, architecture and function of the latch mechanism. According to Ilton et al. (2018), arthropods have evolved various latch mechanisms, based on diverse core principles such as kinetics and geometry (froghoppers and locusts, Burrows et al., 2008; Burrows and Sutton, 2012), physical contact between skeletal structures (trap-jaw ants, Gronenberg et al., 1993; Patek et al., 2006; snap-jaw ants, Larabee et al., 2018; and mantis shrimp, Patek et al., 2007) or multi-scale fluid mechanics (snapping shrimps, Patek et al., 2007). For example, the power-amplified jump of froghoppers and locusts is enabled by the slow co-contraction of two muscles, the flexor and the extensor muscles. The combination of specialized joints and geometry (mechanical advantage) allows the tibia to be maintained in a brace position during slow elastic energy storage until the flexor muscle is inhibited and the tibia extends very rapidly (Burrows et al., 2008; Burrows and Sutton, 2012). Mantis shrimp lock their sclerites in place and co-contract a pair of muscles, which results in the deformation of elastic parts in the exoskeleton. Once maximal muscle contraction is achieved, the muscles relax and the elastic recoil of the exoskeleton generates the powerful strike. Trap-jaw ant lineages have adapted different contact latches and spring systems in their head capsule to snap the mandibles with extremely high accelerations (Larabee et al., 2017), whereas snap-jaw ants combine latch and spring mechanisms in the mandibles, pressing them against each other prior to the strike.

In this paper, we focus on click beetles, which use skeletal structures in the thoracic hinge to brace their body and maintain the brace position while storing energy in elastic body parts (Patek et al., 2007; Zhang, 2013; Abshagen, 1941; Verhoe, 1918). Although the main components of the hinge have been previously described (Patek et al., 2007), the specific morphology enabling the latch has not been previously analyzed in detail. The term 'click beetles' describes approximately 10,000 species worldwide with the unique ability to quickly snap their bodies (Zhang, 2013). Several hypotheses have been proposed to explain the origin and function of this snapping or clicking ability. These hypotheses include that the clicking noise characterizing the latch release may communicate or deter natural enemies (Abshagen, 1941), or that the snap may help liberate the body from its pupation substrate in decaying wood or soil

1

Fig. 1. Three click beetle species studied in this work. (A) *Alaus oculatus* (photo credit: Ophelia Bolmin), (B) *Parallelostethus attenuatus* (photo credit: Eric Rzeszutko, used with permission) and (C) *Melanotus* spp. (photo credit: Ophelia Bolmin). The scale bars on each picture represent 1 cm. (D) The body can be divided into two subunits linked by a hinge, which contains a latch contact of the peg and mesosternal lip. This schematic is adapted from Bolmin et al. (2017). (E) During the pre-jump stage, the peg retracts from the cuticular cavity and latches on the mesosternal lip, moving from the resting position ii to the brace position i. The brace body position is maintained by the peg/lip contact. The motion is reversed when the latch is released.

(Verhoe, 1918; Quelle, 2008; Fursch, 1955). Because the snap as a jump from a horizontal surface does not result in a large lateral distance traveled (typically less than 50 cm) (Ribak and Weihs, 2011), it is unlikely that the jump is effective for escaping predators. In fact, when threatened, click beetles more often appear dead or flee (Ribak et al., 2012). The snap maneuver may also have a signaling or locomotion function to allow for self-righting using a launch into a relatively open area. Regardless of the specific function of the snap maneuver, the complex hinge imparts the high-speed motion to the entire body (Evans, 1972, 1973; Kaschek, 1994; Bolmin et al., 2017).

The click beetle jump has three stages, as previously identified and characterized by Bolmin et al. (2017): the pre-jump, take-off and airborne stages. In the pre-jump stage, the body is supine, and the prothorax is rotated around the hinge (Fig. 2A) until the body reaches a brace position (Fig. 2B); the duration of this is ~2–3 s. In the take-off stage, the brace position is released in a 'snap' fashion, which accelerates the center of mass upward until the body is no longer in contact with the substrate (Fig. 2C,D). The airborne stage is characterized by ballistic motion of the center of mass, which means its path can be fully described by the initial speed and angle of launch (Fig. 2E) (Evans, 1972; Kaschek, 1994; Bolmin et al., 2017).

The initiation of the jump is enabled by the unique interaction of the peg that protrudes from the ventral prothorax and the mesosternal lip at the anterior of the mesothorax (Fig. 1D). During the pre-jump, the peg retracts from a cuticular cavity on the mesothorax, slides up a smooth guide and leans on a conformal lip. This retracted position is a 'latched' or 'brace' position because friction and geometry restrain the peg, bracing the body position while muscles may continue to contract internally. When the friction and geometry restraints are removed, i.e. the peg moves from position i (the brace position) to position ii (the typical resting, non-brace position) in Fig. 1E, the peg slips back over the lip and into the cavity. The fast body rotation accelerates the center of gravity of the body upwards, which, when unconstrained, results in a jump (Fig. 2) (Bolmin et al., 2017).

Even though it has been determined that removal or damage of the hinge mechanism prevents the brace position (position i in Fig. 1E) (Evans, 1972), in this work, we determine specifically how the peg morphology, along with its interaction with the mesosternal
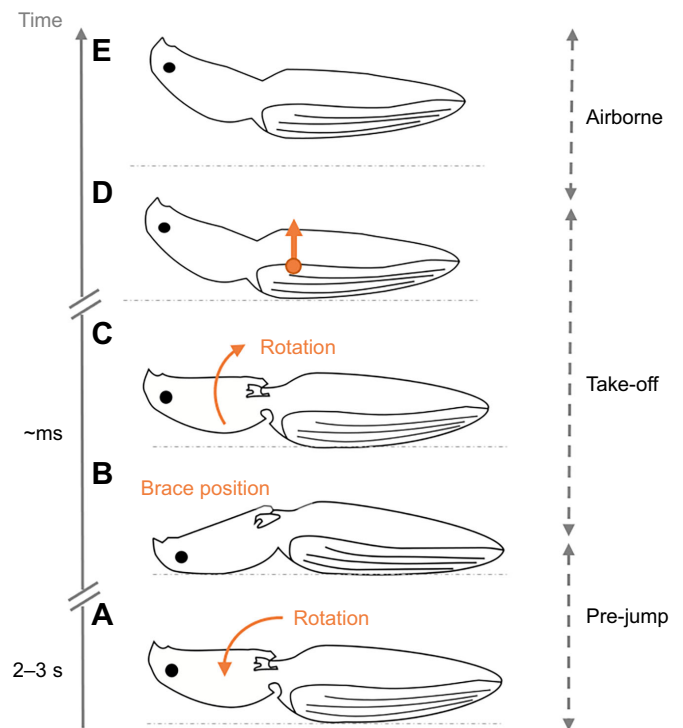
Fig. 2. The observed stages of the click beetle jump, adapted from Bolmin et al. (2017). (A,B) To jump from a supine position, the body arches until a brace position is achieved. (C,D) The take-off stage accelerates the center of mass upward owing to flexion of the hinge. (E) The airborne phase is considered to be ballistic.

lip, gives rise to the brace position. We first describe the anatomy in detail and define the characteristic morphological measurements using environmental scanning electron microscopy (ESEM) and computerized tomography (CT). Micromechanical experiments are then used to measure the force-displacement characteristics of the pre-brace, brace and post-brace positions. Finally, a beam-bending mechanics model is used to quantify the peg-equivalent bending stiffness that maintains the brace position. The critical function of the hinge anatomy is comprehensively described for the first time through an integration of specific anatomical morphology and engineering mechanics.

MATERIALS AND METHODS
Collection, taxonomic assignments and morphology
Beetles were collected in urban and forested sites in Champaign, Piatt and Vermillion Counties in Illinois, Barry County in Michigan and Allen County in Ohio, from private property with the permission of the property owners or from permanent research sites owned by the University of Illinois at Urbana-Champaign with permission from the University's Committee of Natural Areas. Live beetles were collected from April to July 2017. Beetles were manually collected on live trees, at fluorescent lights or by excavating coarse wood debris. Free-flying click beetles were collected in black cross-vane panel traps (AlphaScents, Portland, OR, USA). Panel traps were coated with the fluoropolymer dispersion Fluon® PTFE (AGC Chemicals Americas, Inc., Exton, PA, USA) to improve trapping efficiency (Graham et al., 2010). Traps were modified to capture beetles alive by replacing trap basins with 2-liter plastic jars that had the bottoms cut out and replaced with aluminum screen. Traps were hung ~0.5 m above the ground from tree branches. Lures consisted of polyethylene sachets (press-seal bags, Bagette model 14,772, 10×15 cm, 0.05 mm thick, Cousin Corp., Largo, FL, USA) loaded with 100 ml of 90% ethanol. Traps were checked two to three times per week. Individual beetles were removed and placed in 0.06- to 0.5-liter plastic containers (Dart Container Corp., Mason, MI, USA). Plastic containers contained wood material such as bark and a 1.7-ml microcentrifuge tube (Denville Scientific, Holliston, MA, USA) or 10-ml glass vial filled with 10% sucrose solution capped with a cotton ball.

Beetles were identified to genus, or species when possible. Taxonomy of collected beetles follows Arnett (2002). Voucher specimens were deposited in the Illinois Natural History Survey Insects Collection, Prairie Research Institute, Champaign, IL, USA. Four click beetle taxa from four different subfamilies were collected: *Alaus oculatus* (Linnaeus 1758), *Parallelostethus attenuatus* (Say 1825), *Lacon discoideus* (Weber 1801) and *Melanotus communis* species complex (Gyllenhal 1817).

Specimens in the genus *Melanotus* were identified to a complex comprising seven species that can only be differentiated using internal morphological characteristics, specifically, genitalia (Quate and Thompson, 1967). All species in the *Melanotus* spp. complex are similar in size and shape and overlap in their geographic ranges. Species level identification for the individuals of *Melanotus* spp. did not impede the experimental procedures used in this study. Throughout this paper, we refer to individuals from the complex as *Melanotus* spp.

For this study, the dry mass of each specimen was used as a metric of its size. Desiccation was achieved using an oven (Chicago Surgical & Electrical Co. 300, formerly Chicago, IL, USA) at 28°C for approximately 10 days. Mass was measured every 2 days until stabilization using a Fisher Scientific Accu Series scale (Waltham, MA, USA) with a sensitivity of 1 mg. The dry mass represents approximately half the mass of a live animal. The length of each specimen was determined by adding the length of the two body subunits: the length of the head+prothorax, and the length of the mesothorax+metathorax+abdomen, measured from the base to the apex using Mitutoyo Absolute calipers (Kawasaki, Japan).

Hinge morphology: external and internal imaging
ESEM of peg and mesosternal lip external morphology
Scanning electron micrographs (Philips XL30 ESEM-FEG, at 50 kV; FEI Company, Hillsboro, OR, USA) were acquired in the Imaging Technology Group, Beckman Institute for Advanced Science and Technology, University of Illinois at Urbana-Champaign. Dried specimens of *A. oculatus* ($n=2$), *P. attenuatus* ($n=2$), *L. discoideus* ($n=1$) and *Melanotus* spp. ($n=6$) were attached to aluminum mounts using double-sided carbon tape and silver paint glue (all materials from Structure Probe, West Chester, PA, USA). Sample and stub were sputter coated with 60:40 Au:Pt for 70 s (Desk-2, Denton Vacuum, Moorestown, NJ, USA) before placement into the microscope for imaging. Micrographs were captured of the ventral, caudal and lateral views of the mesosternal lip and of the ventral, dorsal, caudal and lateral views of the peg.

Ventral, dorsal and lateral orientations of the whole specimen and identical views of isolated anatomy (peg, mesosternal lip and surrounding) were used to draw detailed schematics of anatomical morphology and measure dimensions of the key features (see Fig. S1 as an example). We focused on overall shape and on dimensions that are inputs to the mechanical model of the peg. The length of the peg, l_{peg}, is defined as the distance from the apex of the peg to a cross-section where the anatomy widens very rapidly (Fig. S1A); this is used as the length of the beam in the model. The depth of the friction plate, d_{peg}, is defined as shown in Fig. S1B. This quantity defines how the friction plate slips over the lip. The surface area of the friction plate, S, is also described for comparison to overall size metrics like the overall length and dry mass (Fig. S1C). The surface of the friction plate was determined by analyzing dorsal ESEM micrographs of the peg in ImageJ (Schneider et al., 2012).

CT scans of peg cross-sections
CT (CT Lab GX130, Rigaku Corporation, Japan) was conducted on the head and prothorax of 6 specimens in the Microscopy Suite, Imaging Technology Group, Beckman Institute for Advanced Science and Technology, University of Illinois at Urbana-Champaign. Specifically, the pegs of dried *A. oculatus* ($n=1$), *P. attenuatus* ($n=1$) and *Melanotus* spp. ($n=4$) were scanned along their lengths over 57 min to measure the changes in cross-sectional area. Each scan was run at 70 kV and 240 µA with visible fields of view of 5 mm for *P. attenuatus* and *Melanotus* spp. and 20 mm for *A. oculatus*. Grayscale cross-sections of the peg were saved every 0.02 mm of length using the CT-scan image processing software Simpleware ScanIP (Synopsys, Mountain View, CA, USA).

Each CT image was post-processed using built-in functions of MATLAB (MathWorks, Natick, MA, USA). All images for a particular specimen were cropped to the peg cross-section plus some margin to avoid data loss, and then a threshold was set to a particular pixel intensity. The area of each cross-section was computed by summing the pixel area and converting to real length. The conversion factor, in pixels per millimeter, is calculated by measuring the pixel length of scale bars on the image using ImageJ (Schneider et al., 2012) and dividing it by the actual length of scale bar. Further, the distribution of cuticular mass in each cross-section was quantified using the second moment of area, I, and the exponential function was fit to describe the decreasing trend of mass distribution along the

length of the peg toward the distal end. An exponential decay function was chosen because it provided the most accurate fit for all species.

Hinge mechanics: peg analytical model

Based on our postulate that the shape of the peg and mesosternal lip combine to effectively brace the body in preparation for the snap, a mechanical model is required in order to quantify the response of the overall structure to applied forces. The mechanical model assumptions, including linearity, boundary conditions and loading behavior, are based on both the morphology and the constraints of the hinge structure. The peg protrudes posteriorly from the ventral side of the prothorax and has cross-sectional dimensions that are small compared to its length. Those dimensions, along with its growth axially from the prothorax, indicate its structure as a cantilevered beam. From the morphology, the friction plate near the end of the peg is the contact surface with the mesosternal lip and cavity; the other end is fixed to the prothorax. Therefore, we model the peg as a fixed–free Euler–Bernoulli beam with non-uniform cross-section (Truesdell, 1984) (Fig. S2), with an external load applied at the free end. The small deflection of the peg satisfies the assumption of small, linear elastic deformation required to apply the model correctly.

The latching of the peg on the mesosternal lip prior to the snap is analogous to a snap-fit mechanism where an angled end of a beam is pushed over a ledge to snap into a fixed position. In the peg/mesosternal lip latch mechanism, the peg is the beam, the friction plate is the angled end, and the mesosternal lip is the ledge. During the latch process, a perpendicular load at the friction plate must be applied to bend the peg slightly, so that it can reach the brace position. The deflection of the peg perpendicular to its neutral axis is determined by solving the beam-bending model.

The beam-bending model is governed by a second-order ordinary differential equation (Eqn 1), which relates the second-order derivative of the traverse deflection, w, to the bending moment, M, using the coefficients of flexural rigidity. Flexural rigidity is the product of the Young's modulus, E, and the second moment of inertia of the beam, $I(z)$, which is a function of longitudinal position along the peg length, z:

$$-EI(z)\frac{\partial^2 w}{\partial^2 z} = M. \qquad (1)$$

The model is simplified by considering bending and deflection along the dorsal-ventral axis only, or the x-axis in Fig. S2, and by assuming that loading is applied at a point namely at the tip of the peg. Those simplifications lead to an expression for M that is a simple function of the tip load, P, and length, l_{peg} (Beer et al., 1984):

$$M = P(l_{peg} - z). \qquad (2)$$

The traverse deflection along the beam can be expressed in analytical form by substituting Eqn 2 into Eqn 1 and integrating both sides:

$$w(z) = -\frac{P}{E}\iint\limits_{0}^{l_{peg}}\frac{l_{peg} - z}{I(z)}\,\mathrm{d}z\mathrm{d}z. \qquad (3)$$

In this paper, Eqn 1 was solved numerically for the traverse deflection, w, using a MATLAB built-in function, ode45, with appropriate boundary conditions. Young's modulus, E, was determined from Vincent and Wegst (2004). The second moment of inertia, $I(z)$, and the length, l_{peg}, were derived from CT scans and ESEM data (see CT scans of peg cross-sections, above). A higher flexural rigidity, EI, means a more rigid

structure suitable for structural elements. With all quantities in Eqn 1 defined, the peg traverse deflection as a function of the peg length, $w(z)$, was determined. The equivalent bending stiffness of the peg was defined as the ratio of the tip load, P, to the traverse deflection at the tip, w. The equivalent stiffness scales with the inverse of the length cubed, thus we expect the equivalent stiffness to increase as the length of the peg decreases.

Hinge mechanics: measured forces of desiccated beetle hinges

To estimate the applied tip load, P, an experiment was designed to pull the prothorax dorsally, and measure the forces as the body entered the brace position defined by the peg resting in the divot on the mesosternal lip. The set-up for these micromechanical experiments is shown in Fig. 3. First, a nylon thread with stiffness of 940 N m^{-1} was glued to the dorsal side of the prothorax of desiccated specimens of *A. oculatus* (n=2), *L. discoideus* (n=1) and *Melanotus* spp. (n=6) using Original Gorilla Epoxy Glue (The Gorilla Glue Company, Cincinnati, OH, USA). The glue was cured for at least 24 h. The bodies were mounted in foam from the apex up to the base of the abdomen, approximately 1 mm short of the prothorax–mesothorax junction (i.e. the hinge). A small vise compressed the foam against the body until it was observed to be held without moving under mild loads. The hinge began in a flexed position that occurred naturally owing to the drying process. The end of the nylon thread was looped and tied around the end of the force transducer of a custom microscale force measurement instrument (Reale and Dunn, 2017) with a stiffness of 66.157 μN μm^{-1}, a sensitivity of ~10 μN and a maximum force of approximately 200 mN. A Physik Instrumente Translation Stage (VT-80, Physik Instrumente GmbH & Co. KG, Karlsruhe, Germany) with a 150 mm travel range and a resolution of 5 μm translated the mounted body at v=0.25 mm s^{-1}, which first built up tension in the thread, but eventually prescribed a slow dorsal rotation of the prothorax. With the prothorax rotation, the peg moved from the relaxed position to the bracing position (from position ii to position i, as shown in Fig. 1E). Force was measured continuously as an analog voltage from the deflection of the force transducer using a Lion Precision Capacitive Probe (C6-E, Lion
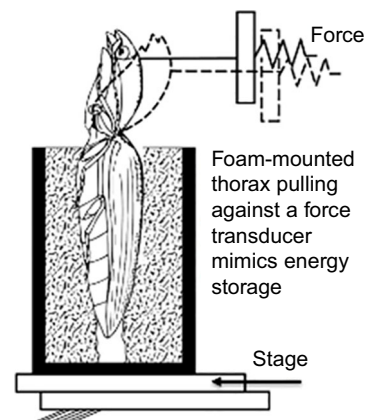
Fig. 3. Schematic of the micromechanical experiment that measures the force drop as the friction plate of the hinge's peg is retracted from the cavity slipping into the brace position against the mesosternal lip. Desiccated specimens were mounted in foam. A nylon thread was affixed to the dorsal side of the head. As the stage moved, the force required to rotate the hinge was measured.

Precision, Oakdale, MN, USA) with a sensitivity of 0.2 V μm^{-1} and an RMS resolution of 3.66 nm. Data were acquired using a data acquisition board (SCB-68, National Instruments, Austin, TX, USA).

RESULTS
Collection and classification
In total, 11 specimens were collected during the summer of 2017. *Alaus oculatus*, the eyed click beetle, is the largest of the four species, with a mean body length of more than 35 mm (Table S1). The smallest species were *L. discoideus* and the individuals from *Melanotus* spp., which were only a quarter of the length of *A. oculatus* (11.3 mand 13.4 mm, respectively) and almost an order of magnitude lighter (13.2 and 26.1 mg, respectively, versus 381.7 mg). The species *P. attenuatus* can be considered of intermediate size as it is larger than *L. discoideus* and *Melanotus* spp., but much smaller than *A. oculatus* (Table S1).

Hinge morphology: external (ESEM) and internal (CT) imaging
The complementary nature of the peg and mesosternal lip for each species is apparent in the conformal sizes and curvatures of these anatomical features. Ventral, dorsal, caudal and lateral views of the peg and mesosternal lip of representative specimens of *A. oculatus*, *P. attenuatus*, *L. discoideus* and *Melanotus* spp. are shown in Fig. 4. All specimens share the following features: a friction plate situated on the peg (I), a conformal ledge on the mesosternal lip (II), a cuticular mesosternal cavity (III) and two rows of hair aligned to the mesosternal cavity (IV).

All specimens investigated have an elongated peg, except for *Melanotus* spp., which has a peg that tapers anteriorly (Fig. 4C). Although the peg does hold the body in a brace position, the smooth, broad surface that faces the interior of the body can be considered a friction plate, or pad, that reduces contact pressure in a sliding interface. The friction plates of all species do not have hairs or follicles, though hairs can be found on the non-contacting side of the peg, facing the ventral side of the body (Fig. 4C).

The mesosternal lip is the anterior edge of the cuticular cavity. As viewed from the lateral side, it shows a concave shape, which appears to exactly match the anterior, convex edge of the friction plate, for all species. The lips of *A. oculatus*, *P. attenuatus* and *Melanotus* spp. all have a central cleft, whereas the edge of the lip in *L. discoideus* appears to have a continuous front (Fig. 4B). In each mesosternal cavity, there are two rows of putative sensory hair, providing a compliant guide directing the peg into the cavity (Fig. 4A). The cuticular cavity is angled toward the interior of the mesothorax such that during most behaviors the peg apex is protected from catching on environmental features (Fig. 4A,B). Furthermore, the peg covers the mesosternal lip, preventing it from trapping debris. Triangular shaped hair pads on the mesosternal lip of *A. oculatus* and *L. discoideus* are observed, but not in the other two species (Fig. 4A, feature V in Fig. 5). Moreover, the orientation of the hair pad appears to be species specific: the pad of *A. oculatus* points towards the ledge and that of *L. discoideus* points in the opposite direction towards the cavity. The function of these common features is further discussed in the Discussion (see Hinge morphology). A large set of micrographs including additional orientations of the anatomy (not shown) were used to draw detailed schematics of anatomical morphology and key features such as the hair pads, and highlight species-specific disparity in shapes and geometries (Fig. 5).

The dimensions of the length of the peg, l_{peg}, the depth of the friction plate, d_{peg}, the surface area of the friction plate, S, as well as overall size metrics (length and dry mass) are presented in Table S2. Based on the current measurements, l_{peg} and S increase with the body length. The ratio of l_{peg} to body length, l_{body}, for all species is between 4.4% and 8.7%. Neither the length ratio, l_{peg}/l_{body}, nor the depth of the friction plate, d_{peg}, follow a specific trend with overall size.

The peg has the largest cross-section at the base, where it protrudes from the ventral prothorax, and the cross-section slowly tapers to a small end; representative images were drawn from five locations along the peg (Fig. 6A), and the corresponding cross-sections (Fig. 6B) show this in detail. Corresponding to this is a
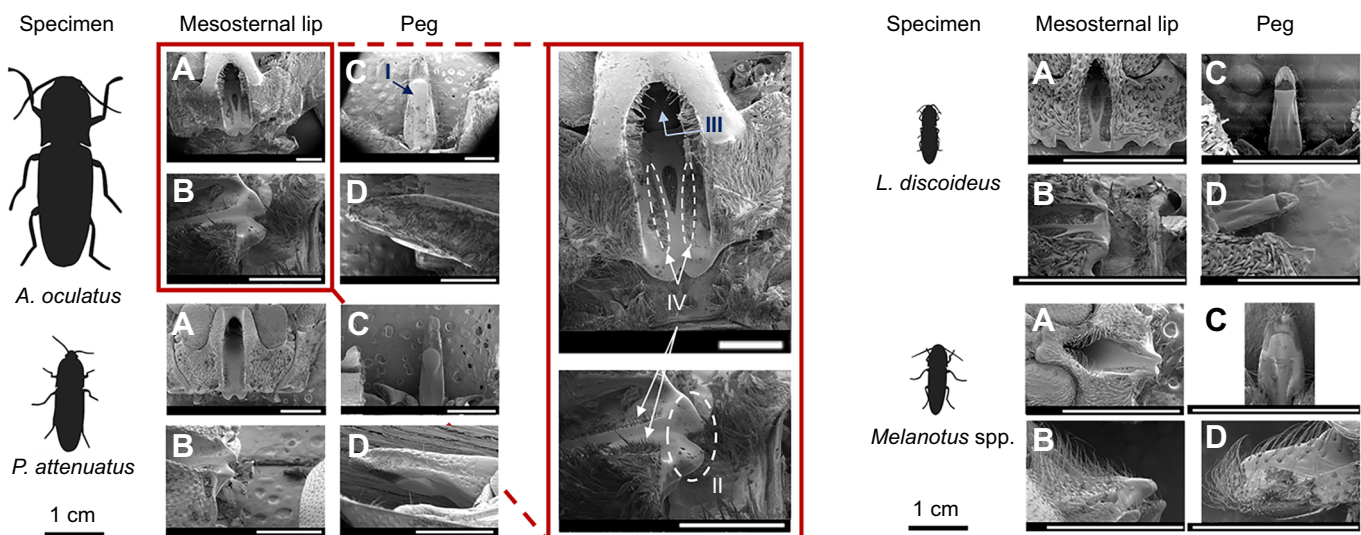
Fig. 4. ESEM micrographs of *A. oculatus*, *P. attenuatus*, *L. discoideus* and *Melanotus* spp. For all species, (A) ventral views of the mesosternal lip and cavity, (B) lateral views of the mesosternal lip, (C) dorsal views of the peg and (D) lateral views of the peg. The white scale bars on each micrograph represent 1 mm. The micrographs show the common features across species: (I) a friction plate on the peg, (II) a conformal ledge on the mesosternal lip, (III) the cuticular cavity and (IV) the rows of hair on the mesosternal cavity. The schematics on the left side of each micrograph set show the overall shape and relative size of the specimens.
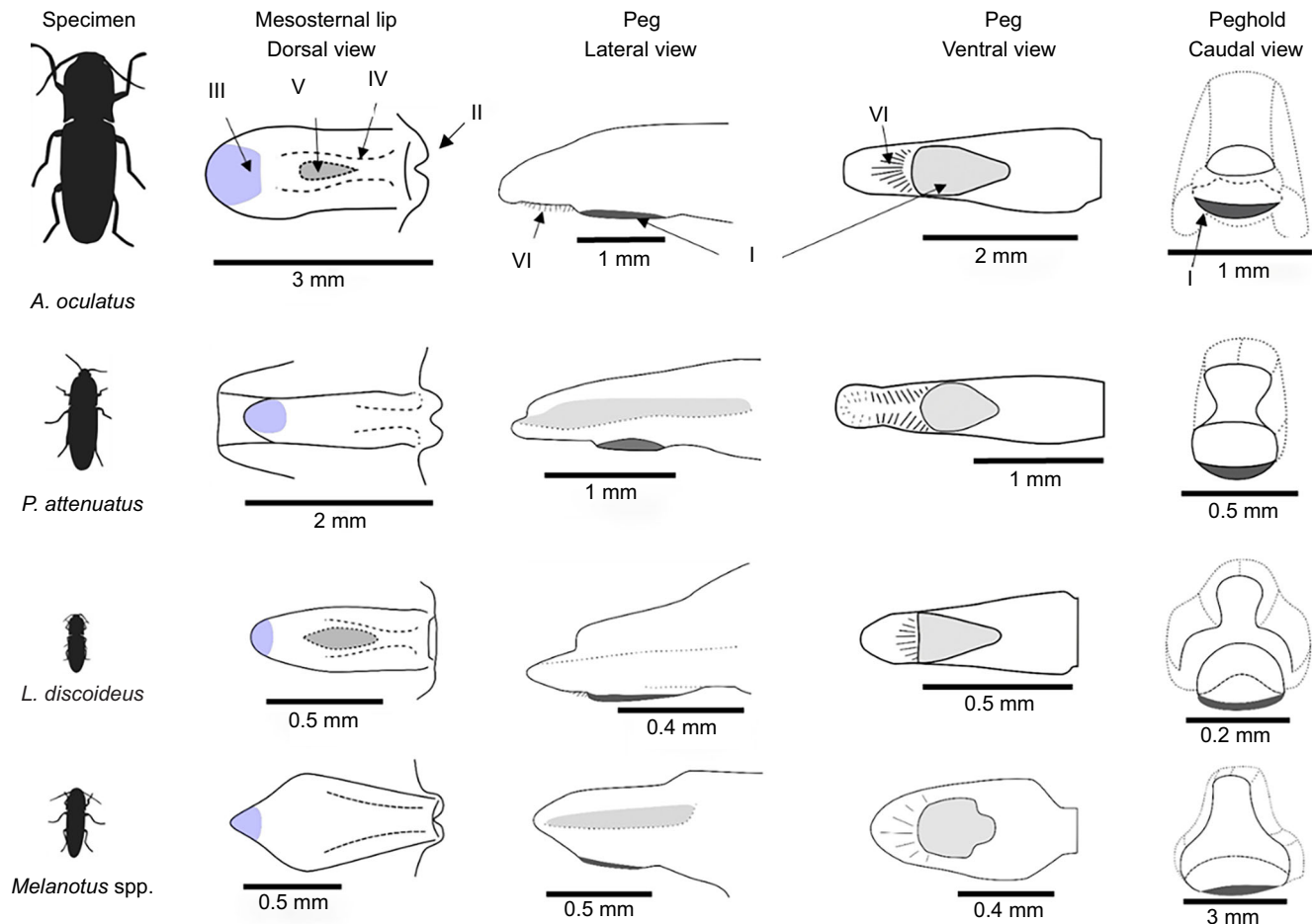
Fig. 5. Schematics of the peg and mesosternal lip of *A. oculatus*, *P. attenuatus*, *L. discoideus* and *Melanotus* spp. derived from the ESEM micrographs. Highlighted features include: (I) the friction plate, (II) the mesosternal cavity, (III) the cuticular cavity, (IV) the putative mesosternal sensory hair guides, (V) the hair pads and (VI) the peg's putative sensory hairs, as well as the overall geometries.

cylindrical cavity identified for the first time – although the resolution of the CT does not allow for clear recognition of its internal contours, the cavity cross-section follows the external size, and vanishes at the distal end. The area moment of inertia, $I(z)$, describes the mass distribution of each cross-section around the neutral axis of the peg. The neutral axis is determined by finding the position in each cross-sectional image of the peg along the dorsal–ventral axis where the material mass above it is the same as that below it. Here, we assume that the density distribution within the peg is uniform. A representative curve of 30 cross-sections from a *Melanotus* spp. individual is shown in Fig. 6C. The data were fitted using an exponential decay function (see Materials and Methods, Hinge mechanics: peg analytical model, for details). The decay constant in the exponential fit is an indication of how quickly the peg tapers. For the representative data, shown in Fig. 6C, the decay constant is -5.01 mm^{-1}. The decay constants for *Melanotus* spp. ($n=4$) and *A. oculatus* ($n=1$) are -3.99 ± 1.99 (mean±s.d.) and -0.53 mm^{-1}, respectively. Normalizing these coefficients by the length gives -2.74 and -1.66 for *Melanotus* spp. ($n=4$) and *A. oculatus* ($n=1$), respectively. These values indicate that *Melanotus* spp. has a larger tapering ratio than *A. oculatus*. For the larger species, the peg appears to be more uniform, though it still exhibits a bending stiffness that is higher close to the connection with the prothorax, owing to cross-section tapering.

Hinge mechanics: hinge force and stiffness

When the peg crosses over the lip in the micromechanical experiment, a force drop was readily observed, and confirmed as to have occurred at the time of peg retraction using video recordings (not shown). A representative force trace of one specimen (*Melanotus* spp.), previously described by Bolmin et al. (2017), is shown in Fig. 7. Initially, the measured force increases monotonically with the deflection applied, then a force drop on the order of 10^{-3} N, or single mN, is observed as the peg slips into the brace position (position ii to i in Fig. 7). At the end of the force trace, a significant drop is observed corresponding to macroscale breakage of the dorsal body junction. This force drop corresponding to the macroscale breakage is an artifact of the experimental setup and is not observed in live click beetles during the pre-jump or take-off phases. During the experiment, the stage motion was not interrupted at the exact moment when the mechanism reaches the brace position. As a result, the peg is retracted even further past the mesosternal lip, leading to complete fracture of the hinge at the dorsal body junction.

The tension buildup, snap-fit force drop and macroscale breakage phases of the force trace were carefully monitored to ensure that the reported force drops correspond to the correct phase. The overall tension rose to a value greater than 200 mN. The force transducer sensitivity of approximately 10 μm allows a reliable measurement
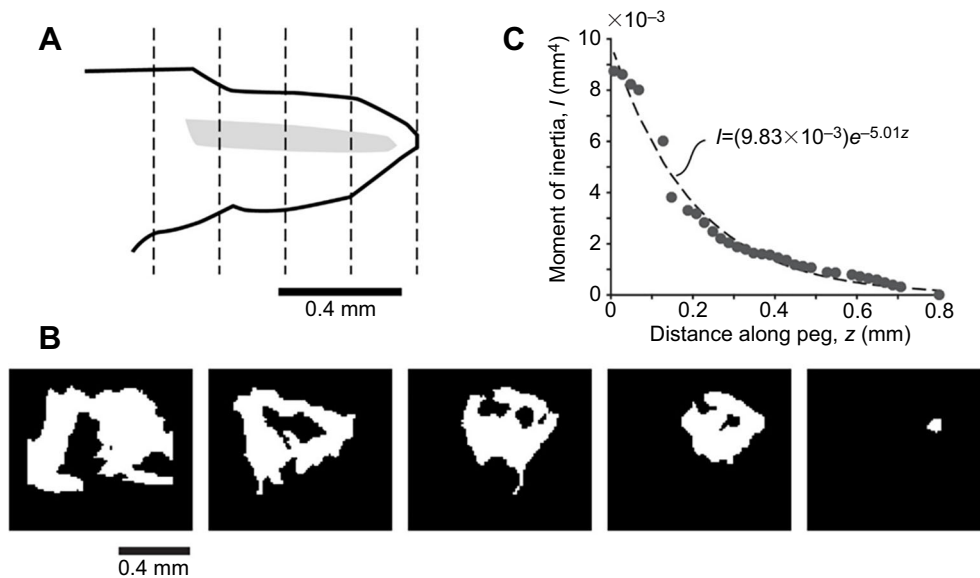
Fig. 6. The rigid pre-jump brace position is accomplished in part by the geometry and stiffness of the peg. (A) The cross-section of the peg along its length determines its stiffness. The cross-section, including interior features, was measured at up to 30 locations along the peg (five of these 30 locations are represented by the dashed lines). (B) Representative CT scan images of a *Melanotus* spp. individual (sample 3, Table 1) were thresholded, and the shape of the solid components is shown in white; near the base of the peg (left image), it has the largest cross-section. An intermediate section is similar in outside diameter with a changing interior cavity, and the smallest cross-section occurs at the end (right image). (C) The area moment of inertia, *I*, is a metric that describes the distribution of mass, which leads directly to the stiffness. The area moment of inertia for all images in the representative samples is shown here; a decreasing area moment of inertia corresponds directly to the decreasing cross-sectional area of the peg. An exponential decay function describes the change in shape.

of the force drop of single mN. The tabulated results of the force drop are shown in Table 1.

The force measurements along with an appropriate mechanical model enables predictions of the stiffness of the pegs, and comparisons of the stiffness within and across species. The force drop measured during the experiments corresponds to the applied tip force, *P*. When these forces are input into the beam model (Eqns 1 and 2) that already includes the specific peg geometry for each specimen, the expected peg deflection *w* can be calculated for all locations along the length of the peg, which begins at the base of the peg ($z=0$) and extends to $z=l_{peg}$ (Fig. 8A). The result is shown as an area rather than a single line because Eqn 1 was solved for a range of Young's modulus, $E=6$–8 GPa, according to Vincent and Wegst (2004). Among the four *Melanotus* spp. specimens tested in the micromechanical experiment, the average force drop is 1.72 mN and the average tip deflection is only 14 nm (Table 1).

The tapered geometry of the peg in conjunction with the internal cavity imparts a unique advantage in structural rigidity, stress management and localized deflections. This is shown by comparing the deflection profile of a beam compared with the peg. The engineering beam was constructed with a length and a uniform, average area moment of inertia identical to that of the peg of a representative specimen (Fig. 8B). The deflections at the tips are the same for both the peg and the engineering beam; however, over a vast majority of the length farther away from the tip, the deflection of the uniform beam significantly exceeds that of the peg. This indicates that the deflection is localized near the end for the peg. The gradual connection between the peg and the prothorax finds an analogy in engineering design in fillets, which serve to minimize any stress concentrations where the size and shape of a component changes drastically. Finally, the slope of the peg curve is steeper towards $z=l_{peg}$, indicating that the end region of the peg where the friction plate is located is more sensitive to applied loads than the base. These features, which manifest from a tapered beam, suggest

that the peg is structured for rigidity and localized response to load. Under loading, the localized deflection prevents elastic strain from being transferred towards the base of the peg, where the maximum bending moment occurs. Thus, it is unlikely for the peg to fail like typical engineering beams due to large applied moments. The equivalent bending stiffness of the peg as a beam is defined as the force drop, *P*, per unit of tip deflection, *w* (Table 1).

DISCUSSION
Hinge morphology
The conformal contact between the peg and mesosternal lip supports the postulate that the brace position enables latching, because the two surfaces have some ability to rotate relative to one another while staying in contact. In engineering terms, this is referred to as a limited-motion, combined rotational and translational sliding bearing. Designing such a mechanism from engineering materials would be very complex, but here, elaterid beetles reliably achieve the function of bracing their bodies until the jump initiates. The friction plate on the peg reduces contact pressure in a sliding interface. In addition, it provides a low-friction surface for efficiency. The rows of hair in each cavity provide a very smooth guide for unimpeded relative motion of the peg and the mesosternal cavity during snap and non-snap behaviors. The function of the hair pads observed on the mesosternal cavity of two species out of the four investigated (*A. oculatus* and *L. discoideus*) remains unclear. Their location on the mesosternal cavity suggests that they are in contact with friction plate when the peg is unlatched (position ii in Fig. 1E) and can provide a means of cleaning the friction plate or act as sensors.

Hinge mechanics and stiffness
The overall stiffness of the peg decreases locally along the length from the base to the distal end owing to the tapered geometry. This stiffness for *Melanotus* spp., calculated as the ratio of the average force drop to tip deflection, is 1.2×10^5 N m^{-1}. This value indicates
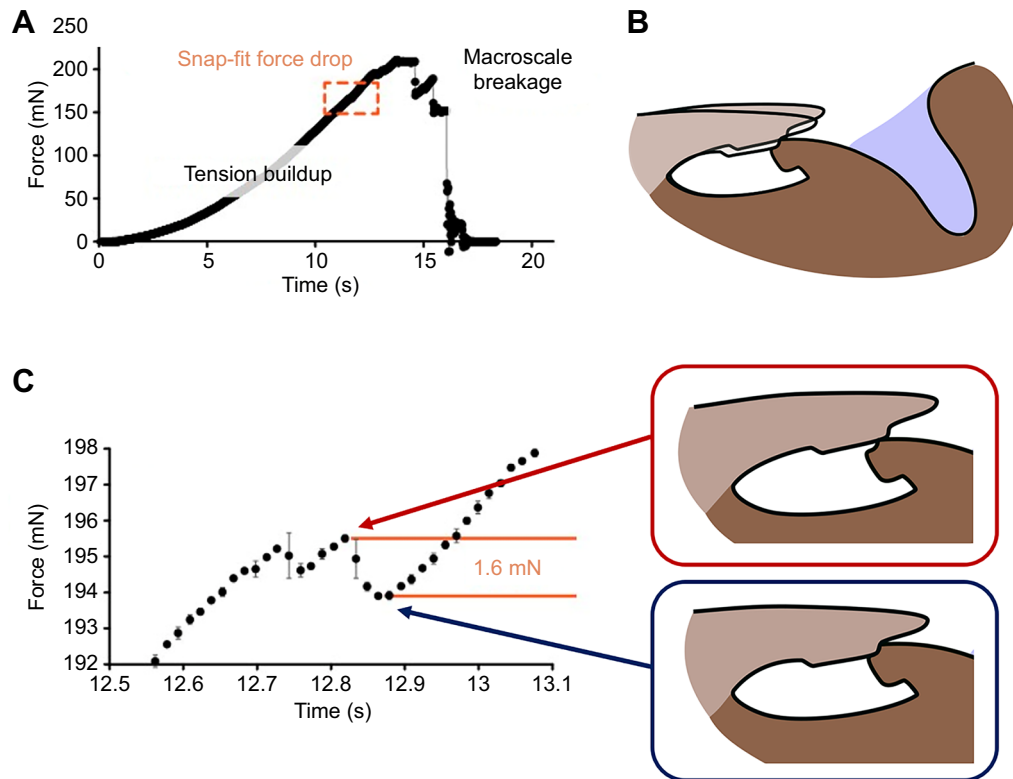
Fig. 7. A representative force response of dorsal flexion in a *Melanotus* spp. individual. (A) The subtle snap-fit force drop and the macroscale breakage are indicated during the initial tension build-up phase. (B) Schematic shows the respective positions of the peg and the mesosternal lip when the force drop occurs. The peg comes to latch on the mesosternal lip, sliding from position ii to position i, i.e the brace position in Fig. 1E. (C) Detailed view of the snap-fit force drop shows a value of 1.6 mN and the respective positions of the peg and the mesosternal lip. The force drop plots in A and C are adapted from Bolmin et al. (2017).

that peg is resistant to bending and provides a strong structure to brace the body before a snap or jump. Although CT data were not obtainable for all specimens, the bending stiffness of *A. oculatus* (n=1) was calculated using similar methods to be 0.45×10^5 N m^{-1}. The stiffness data are plotted against dry mass in Fig. 9. It can be observed that for the specimens studied, beetles of larger size have lower bending stiffness, which agrees with the Euler–Bernoulli beam theory (Truesdell, 1984). According to the theory, bending stiffness is inversely proportional to the third power of beam length, but is linearly proportional to the second moment of inertia. The *A. oculatus* sample peg length is approximately five times the length of all *Melanotus* spp. pegs, but the area moment of inertia decreases by less than 100-fold. Thus, the resulting bending stiffness of the peg of *A. oculatus* is less than that of *Melanotus* spp. It can be concluded that as the peg increases in length, its cross-sectional area

needs to increase to compensate; however, there could be some other reason that restricts the growth in cross-sectional area, resulting in the bending stiffness reduction as the size of the beetle increases. Nevertheless, compared with the growth in mass (approximately 20×), the bending stiffness is decreased by only approximately 4×, and could still function well. This result, along with the variability within the same species shown in Fig. 8B, shows that the performance of snap-fit mechanism can be similar, even though the bending stiffness of the peg varies.

Although this comprehensive investigation has explained more thoroughly how the morphology enables the snap maneuver, some limitations have been identified. Ideally, the micromechanical measurements would accurately capture the force drop at the initiation of the active snap maneuvers. However, during the micromechanical experiment, the beetles are not living, so the

Table 1. Mass and body length, force drop and bending stiffness for the nine specimens

Specimen	Species	Mass (mg)	Length (mm)	Force drop (mN)	Equivalent bending stiffness (N m^{-1})
1	*Alaus oculatus*	404.3	38.8	8.7	N/A
2*	*Alaus oculatus*	359.0	36.5	5.2	$0.45\times10^5\pm0.006\times10^5$
3*	*Melanotus* spp.	28.9	13.4	2.6	$1.03\times10^5\pm0.015\times10^5$
4	*Melanotus* spp.	28.7	13.9	2.5	$1.45\times10^5\pm0.021\times10^5$
5	*Melanotus* spp.	26.8	14.6	0.4	N/A
6	*Melanotus* spp.	25.7	13.5	1.4	N/A
7	*Melanotus* spp.	27.6	13.7	2.1	$2.29\times10^5\pm0.033\times10^5$
8	*Melanotus* spp.	19.1	12.2	1.3	$2.29\times10^5\pm0.033\times10^5$
9*	*Lacon discoideus*	13.2	11.3	0.8	N/A

*Specimens 2, 3 and 9 are the specimens presented in Figs 4 and 5 for *A. oculatus*, *Melanotus* spp. and *L. discoideus*.
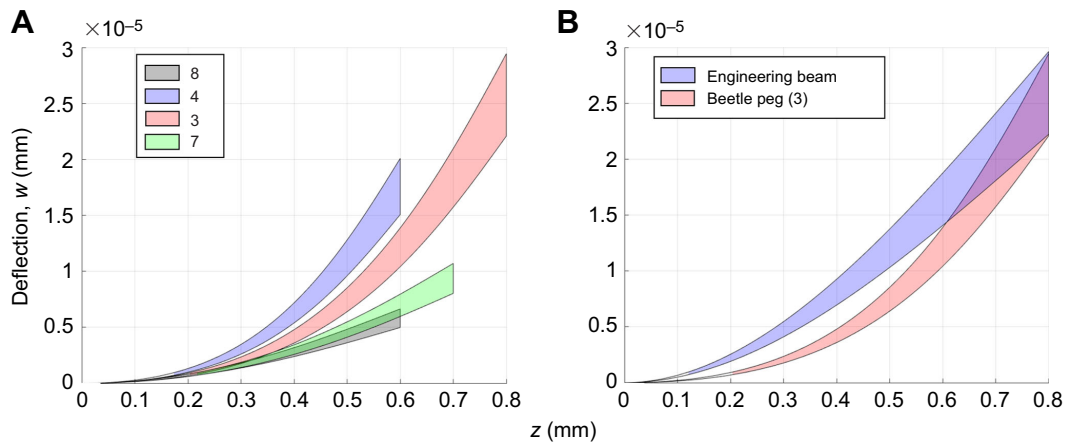
Fig. 8. The deflection of the peg is an indication of its stiffness. (A) Peg deflections of all four individuals from *Melanotus* spp., considering the uncertainty in Young's modulus of insect cuticle. (B) Deflection of a sample peg with point load applied at the tip, compared with a uniform beam of identical average area moment of inertia.

muscle tension and fluid functions that normally exist are disabled. The parameter that is the most affected in the beam-bending model by the drying process is the force drop. Although it is mainly governed by geometry, the force drop value retains some uncertainty. The water content of the hard cuticle is relatively low at ~12% (Vincent and Wegst, 2004), so stiffness changes owing to desiccation are not expected to have a large effect. Moreover, the calculated deflections on the scale of nanometers are very small compared with the friction plate thickness (~50 μm per Fig. 5) or the peg dimension along the dorsal-ventral axis (~100 μm per Fig. 5). This motivates further work to improve the engineering models and measurements, as well as to probe this snap function using *in situ* methods.

Integrated perspective of the latch mechanism
The quick slip of the peg over the mesosternal lip is similar to snapping one's fingers, where a force is applied to a single ratchet and released when the traction force surpasses the static friction force of the interface. Hence, elaterid beetles must have a peg stiffness and peg/lip contact able to maintain the brace position, but also must simultaneously have low friction of the contact in order to slip and snap effectively.
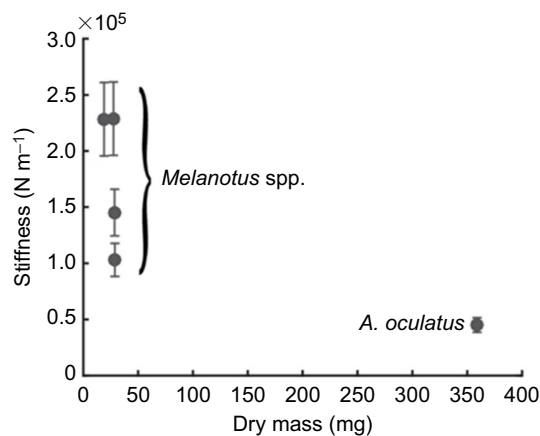
The click beetle's unique hinge anatomy gives rise to engineering interpretations, which support the robust function of the complex hinge in the snapping maneuver. Primarily, the peg/mesosternal lip contact acts as a mechanical latch that holds a brace body position through the conformal contact between the peg and the mesosternal lip. We quantify the bending stiffness of the peg, which allows for very small deformations and enables the latch of the peg on the mesosternal lip.

This work uncovers the specific morphology of the click beetle latching mechanism and uses engineering analysis tools to demonstrate the ability of click beetles to brace their bodies in preparation for the quick-release phase of the clicking/jumping maneuver. The results of this work add to the recently expanding body of literature describing extremely movements in arthropods. For example, the quick snap of the trap-jaw ant operates similarly: a brace position is maintained by the physical contact between two structures, enabling energy storage in elastic elements until some threshold is overcome, and energy is released quickly to snap the mandibles together (Larabee et al., 2017). Other organisms use different latching mechanisms that do not rely on contact between skeletal structures but rather on geometry and kinetics (Ilton et al., 2018). These quick motions have allowed these species to survive by hunting or locomotion in ways unavailable to sister species. Further work on click beetles and other animals with high-speed maneuvers could shed light on selective pressures in this vast order of Coleoptera, and perhaps suggest a search for similar maneuvers in other orders, and how these maneuvers are exploited in the animal kingdom.

Author contributions
Conceptualization: A.C.D., A.W., M.A.; Methodology: O.B., A.M.H., A.C.D., A.W., M.A.; Software: O.B., L.W.; Validation: L.W., A.C.D., A.W., M.A.; Formal analysis: O.B., L.W., A.C.D.; Investigation: A.C.D.; Resources: A.W., M.A.; Data curation: O.B., A.M.H., M.A.; Writing - original draft: O.B., L.W., A.M.H., A.C.D., A.W., M.A.; Writing

Fig. 9. Stiffness versus dry body mass for *Melanotus* spp. and *A. oculatus*. The smaller *Melanotus* spp. beetles, on average, have a peg with a higher stiffness than that of the larger species *A. oculatus*. Error bars indicate the variability based on the range of Young's modulus.

References

Abshagen, K. (1941). Katalepsie und verwandte Erscheinungen bei Kafern. *Z. Wiss. Zool.* **155**, 1-45.

Arnett, R. H. (2002). *American Beetles. Vol. 2, Polyphaga: Scarabaeoidea through Curculionoidea*. CRC Press.

Beer, S. A., Leschen, R. A. and Lawrence, J. (1984). *Vector Mechanics for Engineers: Statics and Dynamics*. McGraw-Hill.

Bolmin, O., Duan, C., Urrutia, L., Abdulla, A. M., Hazel, A. M., Alleyne, M., Dunn, A. C. and Wissa, A. (2017). Pop! Observing and modeling the legless self-righting jumping mechanism of click beetles. Biomimetic and Biohybrid Systems. Living Machines 2017 (ed. M. Mangan, M. Cutkosky, A. Mura, P. F. M. J. Verschure, T. Prescott, and N. Lepora), pp. 35-47. Cham: Springer International Publishing.

Burrows, M. and Sutton, G. P. (2012). Locusts use a composite of resilin and hard cuticle as an energy store for jumping and kicking. *J. Exp. Biol.* **215**, 3501-3512. doi:10.1242/jeb.071993

Burrows, M., Shaw, S. R. and Sutton, G. P. (2008). Resilin and chitinous cuticle form a composite structure for energy storage in jumping by froghopper insects. *BMC Biol.* **6**, 41. doi:10.1186/1741-7007-6-41

Evans, M. E. G. (1972). The jump of the click beetle (Coleoptera, Elateridae): a preliminary study. *J. Zool.* **167**, 319-336. doi:10.1111/j.1469-7998.1972.tb03115.x

Evans, M. E. G. (1973). The jump of the click beetle (Coleoptera: Elateridae): energetics and mechanics. *J. Zool.* **169**, 181-194. doi:10.1111/j.1469-7998.1973.tb04553.x

Fursch, H. (1955). Das Geheimnis der Schnellkafer. *Kosmos, Stuttgart* **51**, 324-326.

Graham, E. E., Mitchell, R. F., Reagel, P. F., Barbour, J. D., Millar, J. G. and Hanks, L. M. (2010). Treating panel traps with a fluoropolymer enhances their efficiency in capturing cerambycid beetles. *J. Econ. Entomol.* **103**, 641-647. doi:10.1603/EC10013

Gronenberg, W. (1996). Fast actions in small animals: springs and click mechanisms. *J. Comp. Physiol. A.* **178**, 727-734. doi:10.1007/BF00225821

Gronenberg, W., Tautz, J. and Holldobler, B. (1993). Fast trap jaws and giant neurons in the ant odontomachus. *Science* **262**, 561-563. doi:10.1126/science.262.5133.561

Ilton, M., Bhamla, M. S., Ma, X., Cox, S. M., Fitchett, L. L., Kim, Y., Koh, J., Krishnamurthy, D., Kuo, C.-Y., Temel, F. Z. et al. (2018). The principles of cascading power limits in small, fast biological and engineered systems. *Science* **360**, eaao1082. doi:10.1126/science.aao1082

Kaschek, N. (1994). *Zoology: Analysis of Complex Systems: ZACS*. G. Fischer.

Larabee, F. J., Gronenberg, W. and Suarez, A. V. (2017). Performance, morphology and control of power-amplified mandibles in the trap-jaw ant *Myrmoteras* (Hymenoptera: Formicidae). *J. Exp. Biol.* **200**, 3062-3071. doi:10.1242/jeb.156513

Larabee, F. J., Smith, A. A. and Suarez, A. V. (2018). Snap-jaw morphology is specialized for high-speed power amplification in the Dracula ant, *Mystrium camillae*. *R. Soc. Open Sci.* **5**, 181447. doi:10.1098/rsos.181447

Patek, S. N., Baio, J. E., Fisher, B. L. and Suarez, A. V. (2006). Multifunctionality and mechanical origins: ballistic jaw propulsion in trap-jaw ants. *Proc. Natl. Acad. Sci. USA* **103**, 12787-12792. doi:10.1073/pnas.0604290103

Patek, S. N., Nowroozi, B. N., Baio, J. E., Caldwell, R. L. and Summers, A. P. (2007). Linkage mechanics and power amplification of the mantis shrimp's strike. *J. Exp. Biol.* **47**, 59-76. doi:10.1242/jeb.052274

Quate, L. W. and Thompson, S. E. (1967). Revision of click beetles of genus melanotus in America North of Mexico (Coleoptera: Elateridae). *Proc. United States Natl. Museum* **121**, 1-83. doi:10.5479/si.00963801.121-3568.1

Quelle, F. (2008). Elateriden-Studien 4 (Coleopt.). *Dtsch. Entomol. Zeitschrift* **2**, 225-229. doi:10.1002/mmnd.19550020503

Reale, E. R. and Dunn, A. C. (2017). Poroelasticity-driven lubrication in hydrogel interfaces. *Soft Mat.* **13**, 428-435. doi:10.1039/C6SM02111E

Ribak, G. and Weihs, D. (2011). Jumping without using legs: the jump of the click-beetles (Elateridae) is morphologically constrained. *PLoS ONE* **6**, e20871. doi:10.1371/journal.pone.0020871

Ribak, G., Reingold, S. and Weihs, D. (2012). The effect of natural substrates on jump height in click-beetles. *Funct. Ecol.* **26**, 493-499. doi:10.1111/j.1365-2435.2011.01943.x

Ribak, G., Mordechay, O. and Weihs, D. (2013). Why are there no long distance jumpers among click-beetles (Elateridae)? *Bioinspir. Biomim.* **8**, 036004. doi:10.1088/1748-3182/8/3/036004

Schneider, C. A., Rasband, W. S. and Eliceiri, K. W. (2012). NIH Image to ImageJ: 25 years of image analysis. *Nat. Methods* **9**, 671-675. doi:10.1038/nmeth.2089

Truesdell, C. (1984). Timoshenko's history of strength of materials (1953). In *An Idiot's Fugitive Essays on Science*, pp. 251-253. Springer New York.

Verhoe, K. M. (1918). Zur Biologie der Elateriden. In *Zur Biologie der Elateriden* (ed. K. M. Verhoeff), pp. 352-359. Sitzungsberichte der Gesellschaft Naturforschender Freunde zu Berlin.

Vincent, J. F. V. and Wegst, U. G. K. (2004). Design and mechanical properties of insect cuticle. *Arthropod Struct. Dev.* **33**, 187-199. doi:10.1016/j.asd.2004.05.006

Zhang, Z.-Q. (2013). Animal biodiversity: an outline of higher-level classification and survey of taxonomic richness (Addenda 2013). *Zootaxa* **3703**, 1-82 . doi:10.11646/zootaxa.3703.1.6